ADVANCED SUSTAINABLE SYSTEMS
www.advsustainsys.com

Responsible Humidity Sensor by Direct Laser Writing on Cork Substrate

Yann Houeix, Denice Gerardo, Sonia Gómez-Gijón, Víctor Toral, Noel Rodríguez, Diego P. Morales, and Almudena Rivadeneyra**

A novel laser-induced graphene (LIG) resistive relative humidity (RH) sensor is successfully fabricated by direct laser writing on a common natural cork sheet. In this work, a straightforward fabrication is presented where LIG, porous multilayer graphene, is generated by a laser photothermal process on a carbon-based substrate, in this case, an agglomerate cork sheet. The formation of LIG material is revealed by structural and morphological characterization using various analyses, including Raman spectroscopy, X-ray Photoelectron spectroscopy (XPS), and Scanning Electron Microscopy (SEM). The electrical analyses are conducted to measure the resulting sheet resistance, getting results as low as 31 Ω sq^{-1}. With the laser parameter optimized, a LIG resistive humidity transducer is manufactured and characterized in a climate chamber. This biodegradable sensor shows good linearity with a sensitivity of 0.015%/%RH from 40 to 80% RH. Additionally, the influence of temperature is studied and demonstrated a low impact on the sensor's response toward RH. Furthermore, a proof of concept is successfully implemented by integrating the transducer onto a cork stopper. Considering all, the prospect of creating an easy, fast, scalable, and cost-effective transducer combined with the use of natural and abundant materials, leads the way for future large-scale production of sustainable sensors.

1. Introduction

Currently, the demand for electronic devices is continuously increasing, presenting new challenges, particularly concerning electronic waste (e-waste) and the scarcity of raw materials. In fact, in 2021, the world generated a striking 57.4 Mt of e-waste, projected to grow to 74.7 Mt by 2030.[1] The improper disposal and recycling of electronic devices have exacerbated pollution, resource depletion, and health risks. Consequently, in response to this fundamental problem, often overlooked by the traditional economic system, the concept of a circular economy is gaining traction. It focuses on sustainability by empathizing with the use of renewable raw and natural resources, maximizing lifetime, prompting reusability, and reforming waste again as resources.[2] As a result, several countries have initiated environmental conservation measures, prompting a shift in numerous manufacturing sectors toward greater eco-friendliness.[3] This evolution is made possible through the adoption of new technologies and materials that have a lower carbon footprint compared to traditional systems.

One interesting and outstanding material is graphene due to its unique properties such as excellent electrical and thermal conductivity, flexibility, and mechanical strength.[4] However, a challenge associated with graphene lies in the complexity of its production and integration, leading to a high cost that acts as a barrier to sensor development. Additionally, the fabrication process of graphene is highly energy-consuming, making it unsuitable for green electronics and raising concerns about its substantial environmental impact when used in devices.[5] New alternatives have spread out such as reduced graphene oxide (rGO)[6] and laser-produced nanographene aggregates originating from polyimide films[7] which have less carbon footprint in the fabrication. This second method consists of a direct laser writing on a carbon-based substrate that, through the laser irradiation, synthesizes a derivative material of graphene commonly known as laser-induced graphene (LIG),[8] laser engraved graphene (LEG),[9] or laser-induced nanographene aggregate (LINA).[10]

Hereinafter we will use the term LIG since it is the one more widely adopted to refer to the carbonization of the substrate by a high-power density laser that breaks out weaker bonds getting a similar structure as graphene at the sub-micron level.[11] This material, created at ambient conditions by the laser, is usually a black conductive foam layer. This method allows for easy mask-free pattern design in a fast and inexpensive way, without any additional treatment. The LIG formation has been reported not only on polymer substrates[12] but also on various carbon

Y. Houeix, D. Gerardo, S. Gómez-Gijón, V. Toral, N. Rodríguez, D. P. Morales, A. Rivadeneyra
Department of Electronics and Computer Technology
Faculty of Sciences
University of Granada
Granada 18071, Spain
E-mail: yannhx@ugr.es; arivadeneyra@ugr.es

The ORCID identification number(s) for the author(s) of this article can be found under https://doi.org/10.1002/adsu.202300606

DOI: 10.1002/adsu.202300606

precursor substrates such as paper,[13] wood,[14] cork,[15] and other sustainable sources.[16,17] It has been stipulated that any carbon precursor is a candidate for LIG.[18] Among natural materials, cork emerges as an interesting candidate due to its abundance, renewability, and biodegradability.[19] Cork is harvested from the bark of cork trees (*Quercus occidentalis* and *Quercus suber*) growing mainly in all Mediterranean regions. This substrate has already been reported for direct laser writing for energy storage,[15] electrochemical sensors,[20,21] and piezoresistive devices.[22]

Among the wide variety of environmental factors, humidity plays a crucial role in biological systems and automated industrial processes. Various types of humidity sensors are available, primarily distinguished by their sensing mechanism, such as capacitive, resistive, or piezoelectric principles.[23,24] The most common measurement is relative humidity (RH), defined as the ratio of the current water vapor content to the water vapor content needed for saturation at a specific temperature and pressure.[25] The utilization of flexible, stretchable, and conformal sensors is expanding across various applications, including the food industry,[26] agriculture,[27] pharmaceutical processing,[25,28] and emerging fields such as health monitoring and human-machine interfaces, where such features are desired requirements for effective implementation.[29] In this context, the recent progress in flexible organic field-effect transistors (FOFETs) has shown significant promise, especially in the development of microcontrollers for flexible electronics.[30] The increasing demand for monitoring the ambient atmospheric conditions with these specified properties has been leading to the development of enhanced RH sensors. These sensors incorporate novel materials, including polymers and composite-based materials, and employ innovative fabrication techniques like screen printing or inkjet printing.[25,31] In this context, there is growing interest in utilizing carbon-based materials from sustainable sources such as cellulose, leaves, and wood because of their rich hydrophilic nature, porosity, and flexibility, making them desirable for sensing moisture content.[32] Several recent studies have explored carbon-based resistive humidity sensors. Fan et al., introduced an RH sensor made of double-layer graphene with an ultrafast response and excellent sensitivity.[33] However, this device involves a complex manufacturing process not suitable for mass production of sensors. Humidity sensors based on graphene oxide (GO) materials have been widely investigated because of the simple, low-cost, and large-scale preparation of GO.[34] Songkeaw et al., demonstrated a transparent and flexible sensor on GO with a rapid response time and the ability to bend over 2000 cycles.[35] Nevertheless, GO is reported to be a toxic material for the environment, discarding it for its use in responsible electronics.[36] Turkani et al., introduced a fast and sensitive RH sensor using carbon nanotubes (CNTs) and hydroxyethyl cellulose as a sensing layer on a silver electrode.[37] Despite featuring a straightforward fabrication technique and enabling a flexible sensor with good sensing capabilities, the use of silver as an electrode restricts its applicability for environmentally friendly sensors. Kulik et al., presented a fully environmental-friendly RH humidity sensor made on paper substrate with fire retardant using LIG, although, its sensitivity is moderate and exhibits temperature dependence.[38] In contrast, the present study introduces the fabrication process of a LIG resistive RH transducer by only direct laser writing of a natural agglomerated cork sheet. The device is entirely biodegradable and cost-effective, as it is produced through a one-step fabrication process on a cork substrate. The resulting transducer exhibits good sensing capabilities and is nearly independent of temperature variations. This work is structured as follows: First, a preliminary study of laser parameters is conducted to find the optimal electrical characteristics for this type of transducer. In particular, an electrical analysis was performed to measure the sheet resistance of the samples manufactured with different laser configurations. Then, structural and morphological analysis with Scanning Electron Microscope (SEM), Raman spectroscopy, X-ray Photoelectron spectroscopy (XPS), Fourier-transform infrared spectroscopy (FTIR) and Thermogravimetric analysis (TGA) was used to supervise the quality and structure of the resulting LIG. Furthermore, a patterned prototype of a cork resistive transducer was fabricated using the technique presented, and its impedance was characterized in a climatic chamber considering the influence of RH, temperature, and working frequency. Finally, we successfully implemented a proof of concept of a transducer onto a cork stopper. This work demonstrates, for the first time, the viability of producing a sustainable RH sensor through laser irradiation of agglomerated cork, achieving comparable or even superior performances to other sustainable sensors reported in the literature.

2. Results and Discussion

2.1. Electrical Characterization

The LIG on the cork sheet is produced at a certain irradiation energy threshold of the laser at which the conductive graphene-derived material starts to form. To optimize the process, LIG samples were systematically produced by changing the optical power and scan speed of the laser in a large range. However, only measurable conductive samples are produced for low powers (0.5–1 W) and low speeds (5–30 mm s^{-1}). For each power applied the minimal speed has to be adjusted to avoid combustion and flame generation of the cork.

Figure 1a shows the test of each sample measured where each column represents laser power from 0.5 to 1.0 W and in each row, the scan speed from 5 to 45 mm s^{-1}. Figure 1b presents the variation of the sheet resistance with respect to the scan speed and laser power. Three distinct formation behaviors are observed, categorized into the high heat-accumulation region (HHR) at <10 mm s^{-1}, the optimized heat-accumulation region (OHR) at 10–20 mm $s^{-1,}$ and the low heat-accumulation region (LHR) at 20–35 mm s^{-1}. At low speeds, increased exposure time results in laser-induced heat accumulation on the cork, leading to thermal-stress-induced microcracks and substrate damage as presented in Figure S1(Supporting Information). Consequently, the electrical conductivity of the LIG is degraded.[39] In OHR, with increasing speed, the thermal effect weakens, allowing for the optimization of electrical conductivity. In LHR, with increasing speed, the sheet resistance of the LIG layer dramatically rises, attributed to the sudden decrease in LIG formation due to insufficient energy density for consistent LIG formation. Finally, beyond 35 mm s^{-1} of scan speed, there is no measurable conductivity, this is because at that speed all the LIG generated is completely removed from the surface and smoke is generated by an abrasive effect of the beam irradiation. At a higher speed, only the residual ashes

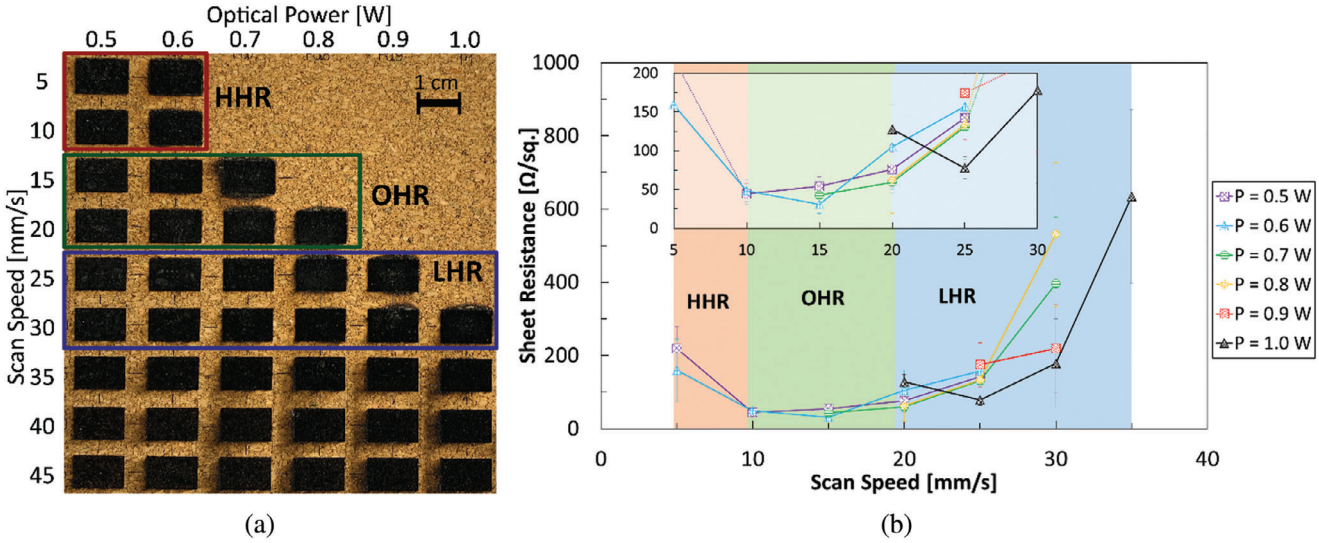

Figure 1. a) Photograph of LIG samples for different laser power and speed conditions. b) The sheet resistance of the measured LIG samples (inset magnified view up to 200 Ω sq^{-1}). Three distinct formation behaviors are observed, categorized into high heat-accumulation region (HHR), optimized heat-accumulation region (OHR), and low heat-accumulation region (LHR).

deposited are present on the surface. Note that the right corner of Figure 1a is left empty since at that high power and low speed the cork starts to burn and generate excessive smoke. Any carbonized sample beyond that point does not provide a measurable conductivity by contact-based techniques.

In this way, the maximum laser power of this setup should be up to 1 W to be able to generate conductive LIG since beyond that power a speed higher than 30 mm s^{-1} is required to avoid any combustion of the sheet. Note that the process for the formation of LIG on the substrate depends on the laser wavelength. For UV laser, the reduction of the material is primarily attributed to the photochemical effect.[22] Alternately, for infrared (IR) lasers the prevailing process is the photothermal effect.[23] Specifically, with a 532 nm wavelength (visible) the photothermal effects prevail for the nanostructuration of LIG on the substrate.

Thus, for this setup, the minimal sheet resistance measured is 30.9 ± 11.9 Ω sq^{-1} for a power of 0.6 W and speed of 15 mm s^{-1}, in the OHR region. In **Table 1**, the LIG sheet resistance obtained in this work is compared with other recent studies of LIG in different raw natural substrates. The thickness of the LIG generated on cork substrate has been measured with an optical microscope by studying the cross-section of a sample, as presented in Figure S2 (Supporting Information) revealing a thickness of ≈ 280 µm, which is in the range of previous works.[21,22]

2.2. Material Characterization

2.2.1. SEM Microscopy

A better understanding of the laser irradiation process can be accomplished through SEM. Originally, before any laser treatment, the cork presents the alveolar structure typical of a vegetal element,[43] as shown on the right in **Figure 2a**. These honeycomb cells have a diameter of ≈20 µm, featuring porous and rugged walls. Upon laser irradiation, the alveolar structures are disrupted, forming visible vertical trenches as depicted on the left side of Figure 2a. The formation process of LIG on cork is different compared to polyimide, where the LIG arises above the precursor surface, on cork it is etched into the material. The distance between these trenches is set at 50 µm and is formed by

Table 1. Comparison of LIG from sustainable sources in recent studies.

Material	Laser	Sheet resistance [Ω sq^{-1}]	Raman [I_D/I_G]	Raman [I_{2D}/I_G]	Reference
Paper	CO_2 @ 10.6 µm	32	0.50	–	[13]
	UV @ 355 nm	125	–	–	[38]
Leaves	UV @ 346 nm	23	–	–	[40]
Wood	CO_2 @ 10.6 µm	10	0.80	0.50	[41]
	UV @ 343 nm	10	0.63	–	[39]
Cork	CO_2 @ 10.6 µm	115	0.50	–	[42]
	CO_2 @ 10.6 µm	10	0.20	0.50	[21]
	UV @ 355 nm	75	0.41	0.37	[22]
	Visible @ 450 nm	46	1.00	0.37	[15]
	Visible @ 532 nm	31	0.34	0.33	This work

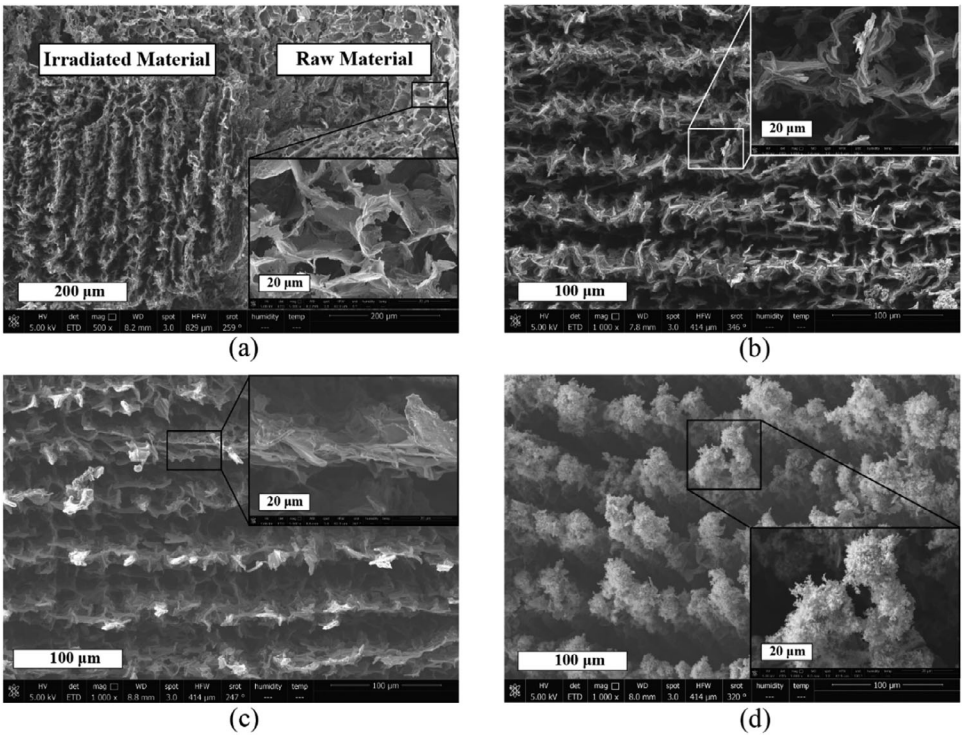

Figure 2. SEM images of a) cork irradiated and non-irradiated zones, b) LIG on cork formed at 0.6 W and 15 mm s^{-1} (OHR), c) 0.5 W and 5 mm s^{-1} (HHR), d) 1 W and 25 mm s^{-1} (LHR).

the overlapping laser passes. Then, the laser irradiation modifies the material from a natural honeycomb structure to a more deformed sponge structure. Detailed observation of the surface with the variation of the laser power is presented in Figure 2b–d. The irradiation energy is proportional to the width and depth of the trench as the alveolar lattice is more damaged by higher laser energy. This is visible comparing the resulting material after irradiation, in Figure 2b (0.6 W, 15 mm s^{-1}) the alveolar structure is still observable, but by increasing the power at a lower speed, Figure 2c (0.5 W, 5 mm s^{-1}) very little of the raw structure is maintained and the trenches are wider and deeper. At the limit just before the combustion, at 1 W and 25 mm s^{-1}, the morphology observed in Figure 2d is drastically different: this is generated by the violent release of smoke, and these particles (the white granular texture in the inset image) get trapped on the skeletal alveolar structure. These facts explain the better conductivity because of the more homogenous and continuous surface formed by intermediary laser power and speed as shown in Figure 1b.

2.2.2. Raman Spectroscopy

The Raman spectroscopy confirms the formation of graphene-derived material. The Raman spectra of different samples are presented in **Figure 3**a showing three main peaks at 1359, 1581, and 2687 cm^{-1}, respectively, D, G, and 2D bands characteristics of graphene-based structures.[44] The D peak is attributed to the defect of the structures and assesses defect in a disordered region of the graphitic structures. The G peak corresponds with the sp2 hybridized carbon network of graphitic material. Finally, the 2D peak formed through the second-order zone boundary two-phonon process signifies the transformation from amorphous carbon to crystalline graphitic carbon.[45] In single-layer pristine graphene, the D peak would be inexistent and the ratio of the intensity of the 2D peak and the G peak (I_{2D}/I_G) is ≈2–3.[46] It is known that the ratio I_{2D}/I_G is dependent on the number of graphene layers, decreasing as the number of layers increases.[47] Consequently, a lower ratio I_D/I_G indicates a higher crystallographic quality of the material, whereas a higher ratio I_{2D}/I_G suggests a greater number of layers. In the HHR region (0.5 W and 5 mm s^{-1}, blue curve), the resulting LIG features a comparable number of defects and a lower number of layers (indicated by a higher I_{2D}/I_G ratio) compared to the sample treated at the OHR (0.6 W and 15 mm s^{-1}, shown in orange). Consequently, the higher crystallographic quality and increased layer count contribute to higher conductivity.[48] However, as the irradiation energy is raised, conductivity continues to increase until a point where the conductivity decreases as the excessive irradiation disrupts the carbon bonds, leading to a rise in defects. Therefore, the resulting material resembles amorphous carbon more than graphene-multilayer, resulting in lower conductivity. This is evident in the case of the samples in the LHR region, represented in red.

2.2.3. XPS Spectroscopy

Further analysis is carried out to understand the process of cork graphitization by XPS spectroscopy. As expected, only carbon and oxygen are the main components of the cork, as depicted

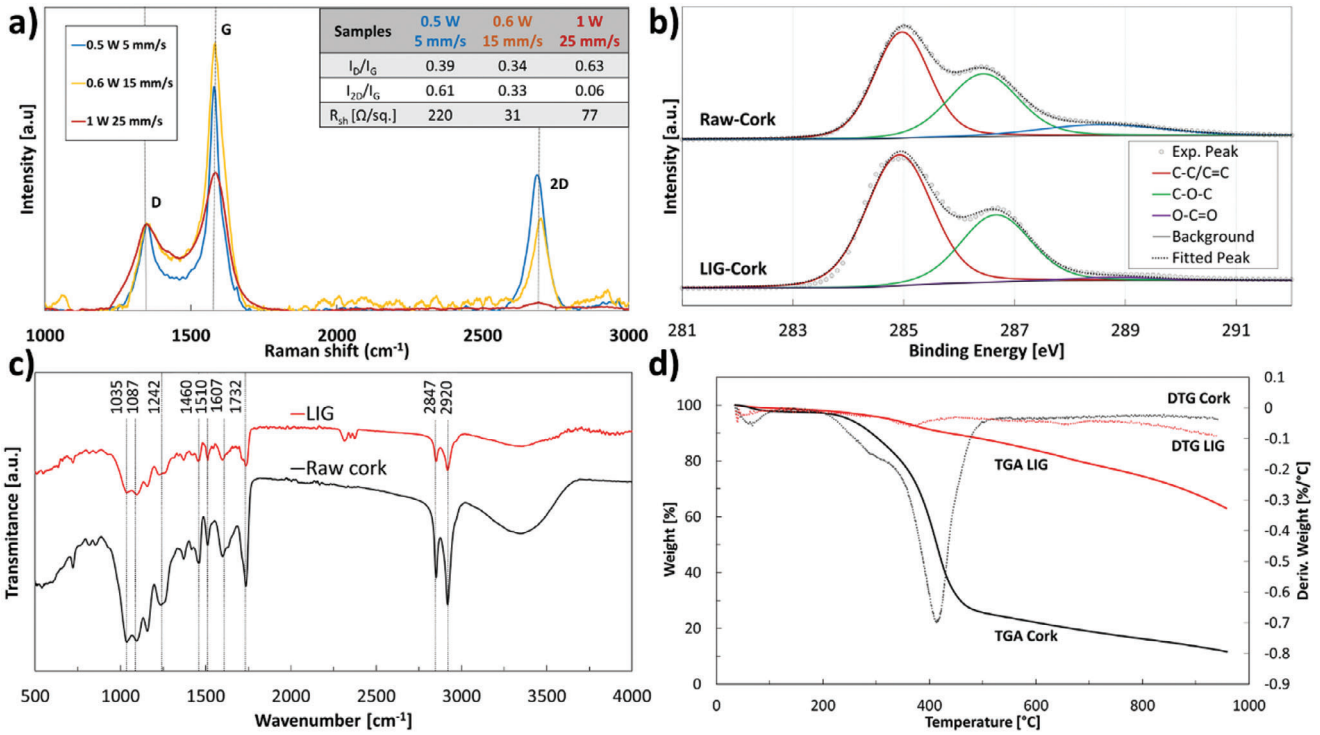

Figure 3. a) Normalized Raman spectroscopy of different samples with the computed ratio between peaks. b) XPS C 1s deconvoluted spectra for the raw cork and LIG material. c) FTIR spectra for the raw cork (black curve) and LIG material (red curve). d) TGA and derived TGA (DTG) curves of cork and LIG under N_2 atmosphere.

in Figure S3 (Supporting Information). Furthermore, Figure 3b displays the deconvoluted C 1s peak for both raw cork and LIG materials. The decomposition reveals three peaks assigned to C—C/C=C, C—O—C, and O—C=O, corresponding to 285, 286.5, and 288.6 eV, respectively.[15]

The raw cork samples consist primarily of highly aromatic compounds, specifically suberin and lignin. The presence of the C—C/C=C peak, representing an overall atomic percentage of 50.6%, is attributed to these principal cork components.[49] After laser treatment, this percentage increases to 63.5%, signifying the conversion from raw cork to LIG. The oxygen component has slightly decreased but is still present and this could be attributed to the partial oxidation of the LIG or the presence of unablated components. Nevertheless, these results align with the trends observed in other carbon-based materials subjected to laser photothermal processes.[12]

2.2.4. FTIR Spectroscopy

Figure 3c displays the FTIR spectra of both the raw cork and LIG material. It reveals an absorption band between 3600 and 3200 cm^{-1}, corresponding to the O—H vibration from carbohydrates and lignin.[50] The spectrum mainly presents absorption peaks of suberin at 2920, 2847, 1732, and 1242 cm^{-1}, assigned respectively to asymmetric and symmetric vibrations, of C–H in the olefinic chains, carbonyl C=O in aliphatic acids and esters and stretch through the epoxide group. Lignin is present in the peak 1460 cm^{-1} (aromatic ring), 1510 and 1607 cm^{-1} (C=C).[15,51,52] Finally, the peaks at 1087 and 1035 cm^{-1} correspond to the C–O bond, characteristic of polysaccharides such as cellulose and hemicelluloses.[52] After the laser engraving process, the FTIR spectrum exhibits a general reduction in all absorption bands, confirming the conversion of cork into reduced graphitic carbon.

2.2.5. Thermogravimetry Analysis

TGA is performed on the natural cork substrate and the LIG one to understand the thermodegradation behavior of both materials and identify associated temperatures for chemical processes. Figure 3d depicts the TGA and DTG curves for both materials. The decomposition process is divided into four stages. The initial stage, extending from room temperature to 200 °C, is attributed to the complete elimination of moisture content.[52] The second region, up to 300 °C, corresponds to the decomposition of polysaccharides, comprising cellulose and hemicellulose, generating gases and oxidation products that induce a darkening of color in the cork.[53] In this region, suberin and lignin also commence degradation to a lesser extent, given their higher thermal stability relative to other elements. The third region is primarily represented by the 412 °C peak on DTG associated with the complete degradation of the suberin and lignin.[15] In the final region, above ≈500 °C, the remaining material undergoes conversion into stable graphitic carbon (≈11%) persisting at higher temperatures >900 °C.

On the other hand, the TGA of LIG material exhibits a higher thermal stability, with 63% of the material stable above 900 °C.

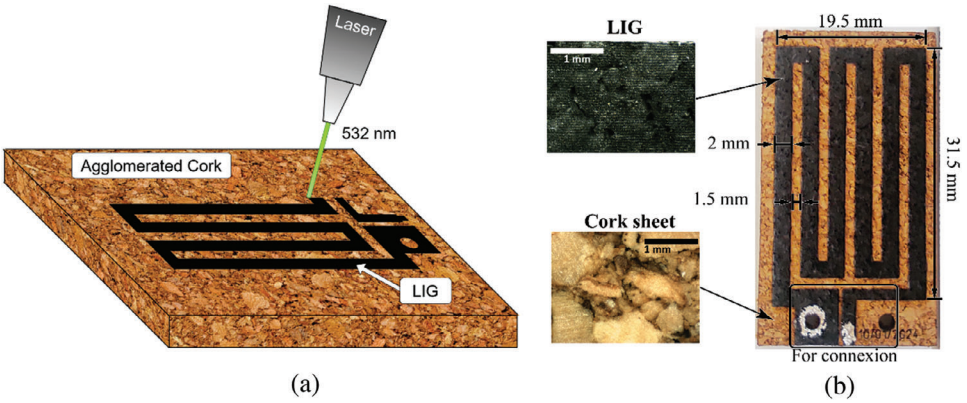

Figure 4. a) Schematics of the traducer fabrication. b) Photograph of the resistive LIG RH transducer with its dimension.

The mass loss for LIG is primarily attributed to the degradation of the residual lignin and suberin still present in the LIG mechanically removed from the cork substrate, as shown in the small peak over 350 °C on the DTG curve for LIG. This further demonstrates the graphitization of the LIG.

2.3. Sensor Characterization

The cork transducer fabrication is depicted in **Figure** 4a. The resistive pattern is formed by direct laser writing on the surface of the agglomerated cork, without any previous treatment or mask. The layout and associated dimensions are presented in Figure 4b. The design features a meander shape to increase the resistance and the effective surface of the transducer, obtaining a total active area of 380 mm^2. At the base, two holes and a large square were included for the Sub Miniature version A (SMA) screw panel mount connector, ensuring a secure and precise attachment of the sensor. Additionally, silver ink is employed to enhance the contact between the connector and the LIG surface. Various prototypes were produced to achieve a highly porous structure using laser parameters of 0.5 W and 5 mm s^{-1}. It has been observed that the sensors are very sensitive to RH due to their increased porosity. However, this high porosity and fissures led to rapid deterioration over time of the sensor response. Consequently, 8 prototypes were manufactured at 0.6 W at 15 mm s^{-1}. The selection of these laser parameters ensures a more uniformly porous surface with fewer fissures and a high-quality LIG structure, as part of the previously described optimization process.

In the magnified section of Figure 4b, the LIG presents parallel lines formed by the laser path, and the granularity of the surface is still visible. However, despite the surface irregularities resulting from grain presence, the LIG surface operates as a continuous conductive material after the laser photothermal effect. Additionally, the agglomerated cork is ideal for more uniform LIG material as its multi-granular structure averages different cork properties and orientations. In contrast, natural cork exhibits anisotropy due to the orientation of the alveolar structure during the growth of the tree.[22] The porosity of the material is a key characteristic of RH sensors, as the porous density and size directly determine the ability of the material to absorb and maintain water vapor.[54] In this case, LIG on cork has a high specific surface because of the high pore density, which enhances the moisture permeability.

The humidity response curve of the cork transducer at different temperatures is shown in **Figure** 5a. LIG sensor exhibits a positive humidity coefficient, where the resistance increases proportionally to the humidity. The sensor demonstrates an average sensitivity of the sensor of 0.015 ± 0.004%/% RH, computed by using Equation 2. Across the entire humidity range (40–80%), the linearity stands at R^2 of 0.83, while within the 40–70% RH range, it reaches a linear coefficient of 0.99. The second-order polynomial approximation for the whole range is slightly better obtaining R^2 of 0.97. Additional detailed information is available in Table S1 (Supporting Information). Furthermore, the effect of the temperature is negligible up to 40 °C, although at elevated temperatures and increased humidity, the deviation rises. Figure 5b presents the temporal variation of the sensor for two cyclic humidity levels across a broader humidity range. The transducer follows the imposed trend, however, at high humidity (≈90%), significant oscillations are observed, which can be explained by the saturation of the sensor.[55] Furthermore, there is a noticeable drift between the increase and decrease of RH because of the inherent nature of the sensor, as further explained below. This drift can be assessed in Figure 5c, presenting the hysteresis, where the maximum value occurs at 75%RH with a deviation of 10.7%. The transient response of the proposed transducer is depicted in Figure 5d, showing a rising time of the sensor of 140 s and a falling time of 177 s, with a 14.8% drift at the end. One potential technique for speeding this process involves incorporating a heater with LIG to increase the temperature on the surface, thereby enhancing the release of water vapor.[56,57] Additionally, as presented in Figure S4 (Supporting Information), the sensor exhibits consistent long-term stability, with a relative deviation of 2.5% over extended periods (≈60 h).

Based on these findings, the sensing mechanism of the cork transducer can be inferred. As illustrated in Figure 5a, a consistent increase in resistance is observed with the rise in moisture content. This observation suggests that the main contributor to the humidity response is the swelling of cellulose on the cork, leading to an enlargement of the grain size.[58,59] This, in turn, results in an increased separation between the conductive carbon-based elements, disrupting the percolative conductive network. Hence, this explains the sensor's slow response

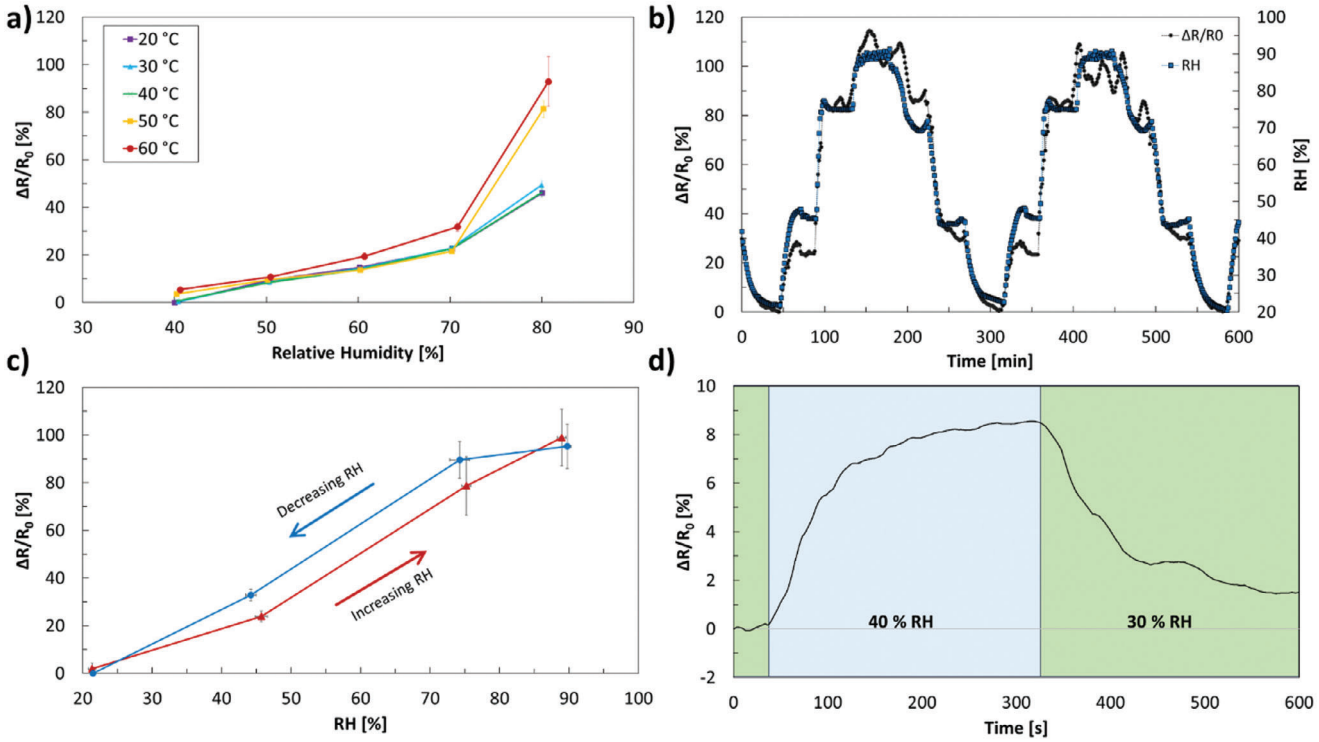

Figure 5. a) Variation in resistance with respect to RH at different temperatures. b) Dynamic response over wide change RH of two cycles. c) Static response of the transducer over increasing and decreasing RH variation. d) Response and recovery time of the LIG sensor.

and hysteresis, as this mechanism is a gradual process dependent on ambient evaporation, which is commonly seen in other RH sensors.[38,60] Similar mechanisms have been proposed in previous works involving conductive carbon-based materials on paper.[38,61,62] Other factors, such as the doping effect and intercalation of water molecules, might play a secondary role in the response to both RH and temperature.[63,64] In comparison, Kulik et al., presented a similar research work involving the development of a temperature and humidity sensor on cellulose utilizing LIG.[38] The study asserts that their sensor is primarily influenced by the swelling of cellulose fibers in the paper induced by humidity, leading to separation on the LIG conductive surface and consequently increasing the resistance of the sensor. Although their sensor demonstrates temperature dependence, this difference can be explained by the porous and heterogeneous nature of our cork substrate compared to the uniformity of the cellulose fibers in paper, as evidenced in SEM images. The granular surface of the cork makes it more susceptible to swelling compared to the change in the resistivity of the LIG due to other effects, rendering it effectively independent of temperature. Furthermore, the paper-based sensor shows a significantly lower humidity sensitivity, over ten times less. **Table 2** presents recent work of resistive carbon-based humidity sensors. In comparison, our transducer exhibits moderate sensitivity and moderate response time while showing minimal temperature dependence. This characteristic is crucial for the RH sensor as simplifies the sensor by eliminating the need for calibration or compensation techniques to mitigate the impact of temperature on sensor response. Other sensors in the comparison use non-renewable materials and different fabrication techniques, yielding similar performances.

Table 2. Comparison of characteristics of recent resistive carbon-based humidity sensors.

Sensitive material	Fabrication process	RH Range [%]	T [°C]	Sensitivity [%/RH%]	Response/Recovery time [s]	Reference
Graphene	CVD	20–100	25	0.85	0.6/0.3	[33]
rGO/Ws	Spraying	0–92	25	1.9×10^{-3}	31/95	[65]
CNF/CB/T X 100	Screen printing	30–90	25	0.02	10/6	[66]
FMWCNT/HEC	Screen printing	20–80	25	0.048	20/35	[37]
PI/GO	LIG	11–97	25	1.12	35/2	[67]
Cellulose	LIG	10–90	10–60	1.3×10^{-3}	95/630	[38]
Cork	LIG	40–80	20–60	0.015	140/177	This work

Chemical Vapor Deposition (CVD).

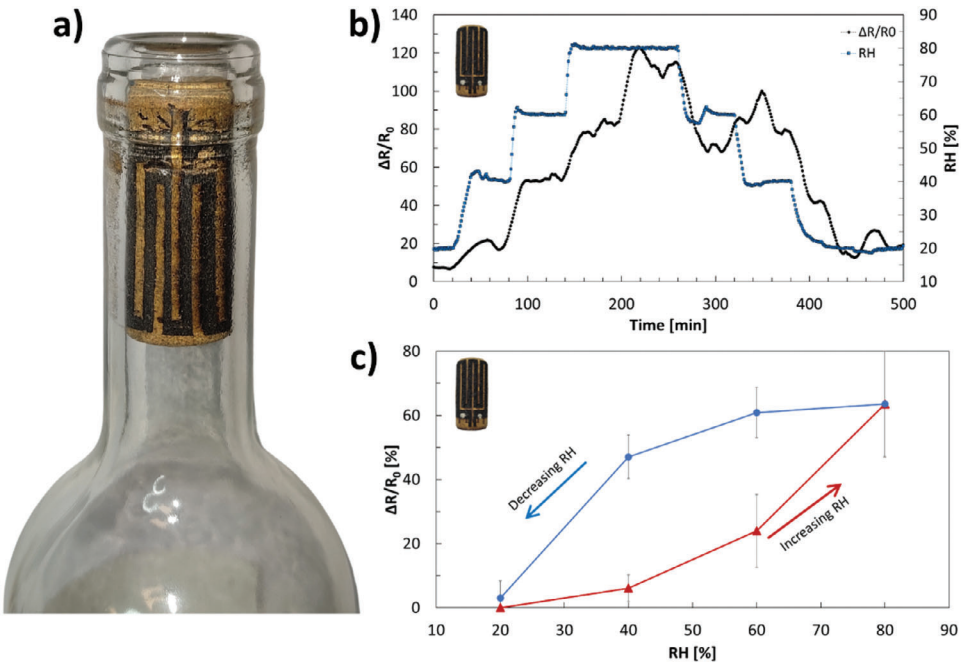

Figure 6. a) Proof of concept of a cork-stopper RH sensor on a bottle of wine. b) Dynamic variation of the transducer over RH variation. c) Static response over increasing and decreasing RH variation.

Therefore, our LIG-cork transducer coupled with its biodegradable capability and straightforward, cost-effective production, stands as a promising choice for environmentally friendly humidity sensors.

The flexibility of the cork sensor was evaluated by bending it with a curvature of 20° as illustrated in Figure S5 (Supporting Information). The results show a 41% decrease in resistance during compression and a 75% increase in resistance during elongation. This behavior is attributed to the compacting of the LIG surface during compression, leading to lower resistance, and the separation of the LIG conductive zone during elongation, resulting in increased resistance.[22] The robustness of the sensor was also tested over 300 cycles of both elongation and contraction. After the elongation cycles, the resistance increased by only 0.4%, while after the compression cycles, the resistance increased by 18.6%. Although, the value stabilizes and reaches 90% of the final value only after 125 cycles. The difference between elongation and compression can be attributed to the definitive disruption and displacement of LIG layers during compression, which stabilizes after some cycles.

2.4. Sensor Application

The integration of LIG resistive RH transducers onto cork presents promising applications in various domains, particularly in areas such as smart packaging and food storage. In the context of food storage, this innovative method can be easily applied to cork stoppers in the wine industry. Deviation in humidity levels detected by the transducer could serve as early indicators of compromised sealing, foreseeing potential adverse effects on wine quality, such as oxidation or spoilage. Additionally, it can evaluate the degradation in the mechanical properties of the cork stopper and its integration allows for continuous monitoring, ensuring the sealed integrity of the bottle.[68] The simple integration during the fabrication of the cork stopper ensures compatibility with traditional wine storage practices.

As a proof of concept, we applied the same engraving technique directly to a commercial agglomerated cork stopper, as illustrated in **Figure 6a**. It is important to highlight that, although the sensor design remained the same, the curvature of the cork stopper was not considered in the design and fabrication processes. This oversight resulted in deviations on the sides, and due to the variable focus length of the laser, LIG uniformity across the transducer is not ensured. The dynamic response of the cork stopper transducer is detailed in Figure 6b,c, showing a trend similar to the previously presented results, however with a lower calculated sensitivity of 0.01%/RH% and hysteresis, reaching a maximum deviation of 41% at 40%RH. Notably, during high humidity and decreasing phases, oscillations and unexpected results are observed. These discrepancies can be attributed to several factors. The cork of the stopper differs from the one used in the other sections of this work, and no further information on its characteristics and possible treatments is available. Additionally, the performance of stoppers depends on their type, showcasing diverse chemical and physical properties.[69] The curvature of the stopper affected the pattern scribed and subsequent LIG formation. The thicker cork and mechanical compression of the cork stopper potentially reduce the swelling mechanism, amplifying hysteresis. However, such variations might not be critical in this application, given the slow and gradual humidity changes in wine cellars. Therefore, these results prove the feasibility of a LIG-cork RH sensor integrated directly on the bottle stopper.

3. Conclusion

In this study, LIG on cork has been demonstrated for the fabrication of sustainable resistive humidity transducers. LIG was formed on an agglomerated cork sheet by the photothermal effect of the laser irradiation with a wavelength of 532 nm without any previous treatment. The formation of the LIG has been characterized by two processing parameters of the laser: optical power and the scan speed of the beam. The samples have been electrically analyzed and the main observation is that the optimal laser condition to get high conductive and homogeneous LIG was at low speed and maximum power at the limit before combustion of the substrate, obtaining sheet resistance as low as 31 Ω sq^{-1} The laser treatment has turned the vegetal hexagonal structure of the cork into a more heterogeneous black foam with a porous structure. Its structure has been characterized by SEM microscopy, Raman spectroscopy and other techniques, proving the formation of graphene-derived material.

The laser has been used to create the meandered pattern for the RH sensor and the devices have been evaluated in real conditions of temperature and humidity. The use of LIG on cork has proved effective in fabricating resistive RH sensors, demonstrating good thermal and electrical responses comparable to other sensors in the field. The manufactured transducers have exhibited an excellent sensitivity of 0.015%/RH% with a very fast time response. Additionally, it has been demonstrated the low dependency of the temperature and the long-term stability of the devices. These remarkable findings, exemplified by the successful proof of concept of a transducer on a cork stopper, pave the way for innovative sustainable sensors, characterized by their incredible combination of biodegradability, flexibility, and cost-effectiveness. This alignment perfectly meets the requirements of circular economy and sustainable devices.

4. Experimental Section

Materials: A commercial agglomerate sheet of natural cork was purchased from Criscolor (Valencia, Spain) and used without any treatment or the addition of any fire retardant. The sheet thickness was 2 mm and with a density of grains of ≈100 grains by cm^2. The cork stopper was obtained from a bottle of Rioja El Coto 2023.

Material Characterization: The optical image features were captured by an optical microscope, LED 69T (Hsinchu, Taiwan) with an adapted camera, Moticam 5+ (Hong Kong, China).

Surface morphology was studied by an ambient scanning Electron Microscopy, ESEM Quanta 4000 (Hillsboro, Oregon, USA), using secondary electrons with a working distance of 8 mm and 5 kV of acceleration voltage, otherwise noted.

Raman spectrometer analyses were carried out by the Micro-Raman Jasco NRS-5100 (Easton, PA, USA) system, using a green diode of 532 nm as the excitation source. No attenuation was performed as the laser power is minimal, therefore not increasing the ablation of the material.

The XPS was carried out on a Kratos Axis Ultra-DLD (Manchester, UK), using an X-ray (Al Kα, $h\nu$ = 1486.6 eV) power of 450 W in a vacuum chamber where the pressure was kept below 10^{-10} Torr. The samples were dried for one day in an oven at a 40 °C chamber before XPS analysis and the spectra were analyzed with CASA software with reference to adventitious C_{1s}, at 285 eV.

The FTIR was performed by JASCO 6200 (Easton, PA, USA), and the spectra were analyzed with SPECTRA MANAGER v2 software.

The TGA/DTG curves were obtained by METTLER-TOLEDO mod. TGA/DSC1 (Barcelona, Spain). The temperature range was set from 35 to 950 °C with a temperature ramp of 10 °C min^{-1} under N_2 atmosphere.

Keysight B2902A Source Meter Unit (SMU) (Santa Rosa, California, USA) was used to measure voltage and current for the electrical characterization of the LIG sheet resistivity together with the four-probe station, Universal Probe Station from Jandel (Eggington, UK) with a spacing between needle of 1.0 mm. The method to evaluate the sheet resistance used was the In-Line Four-Point Probe with the Dual-Configuration described in ref. [70]. This method allows for eliminating the contact and wire resistance and performs high-precision measurements without requiring any form factor due to the sample size.

Sensor Fabrication: The pulsed galvanometric laser used for the scribing process was the PowerLine E-12-532 from Coherent (Munich, Germany). It features a wavelength of 532 nm (green light) and optical power of up to 6 W. The main laser parameters studied were the optical power of the laser, in a range from 0.5 to 5 W, and the speed of the beam, in a range from 5 to 2000 mm s^{-1}. The rest of the laser parameters were the following: pulse frequency of 50 kHz, the distance between two passes of 50 µm, focal distance set 270 mm (optimal distance) obtaining a laser spot of 1.6 ± 0.2 mm.

The LIG was directly formed by laser irradiation on the surface of the cork sheet at ambient conditions and without any previous treatment or mask. The shape design was made using Visual Laser Maker. The active area of the designed transducer was 380 mm^2 and is connected with the measurement unit by a SMA Series End Launch Connect from Bulgin (Santa Fe, CA, USA). To enhance the connection between the cork sensor and the connector, a thin layer of RS PRO conductive silver lacquer is applied near the edge of the connector, as illustrated in Figure 4b.

Sensor Characterization: The impedance of the humidity transducer had been characterized from frequencies of 500 Hz to 1 MHz with the impedance analyzer Keysight E4990A (Santa Rosa, California, USA) and the impedance probe Keysight 42941A from the same vendor. The transducer exhibits a resistive response, therefore, the impedance value used was obtained at 500 Hz. Additionally, the complete frequency response of the sensor is presented in Figure S6 (Supporting Information). The climate chamber used to test the sensor was Weiss Technik, LabEvent L C/34/70/5 (Reiskirchen- Lindenstruth, Germany). For the RH and temperature response, the sensor was placed into the climate chamber where the humidity was increased from 40% to 80% in steps of 10% lasting 8 h. Concurrently, for each humidity step, the temperature was increased and then decreased, from 20 to 60 °C and vice versa, in 10 °C intervals, each lasting 1 h. These values were selected to cover the operational range of the climate chamber and to ensure the stabilization of the environment within the chamber. Furthermore, the cyclic wide range of humidity was set at 20, 45, 75, and 90% RH at a constant 40 °C with each step lasting 45 min for 10 cycles. The measured resistance is expressed as:

$$\Delta R/R_0 = \frac{R_{RH} - R_0}{R_0} \quad (1)$$

where R_{RH} is resistance in different testing RH, and R_0 is resistance at the lower RH. The sensitivity is mathematically calculated using the expression of[37] as:

$$S = \frac{\Delta R/R_0}{RH_f - RH_i} \times 100\% \quad (2)$$

where RH_i and RH_f represent the initial humidity and the final humidity. The time response and recovery time of the sensor were evaluated using the Keithley 2450 SMU (Oregon, USA). The initial conditions included a humidity level of 30% at 25 °C, followed by a rapid increase to 40%. For recovery time, the conditions were reversed. For the aging characterization of the cork sensor, it was placed in the climate chamber with a constant 30% RH and 30 °C for a duration of 58 h. The bending response was continuously measured using the Keithley 2450 SMU. The procedure involved bending the sensor to 20 degrees and releasing it, with each bending

cycle lasting ≈1 s. This process was carried out for both compression and elongation, as illustrated in Figure S5 (Supporting Information).

Supporting Information

Supporting Information is available from the Wiley Online Library or from the author.

Acknowledgements

This work was partially funded by the Spanish Ministry of Sciences and Innovation through the National Projects: PID2020-117344RB-I00, CNS2022-135915, TED2021-129949A-I00 funded by MCIN/AEI/10.13039/501100011033; and the Ramón y Cajal fellow RYC2019-027457-I. It was also supported by the Andalusian regional project P21_00105 through FEDER funds. Funding for open access charge: Universidad de Granada / CBUA.

Conflict of Interest

The authors declare no conflict of interest.

Data Availability Statement

The data that support the findings of this study are available from the corresponding author upon reasonable request.

Keywords

biodegradable material, cork, laser-induced graphene, sensor

Received: November 28, 2023
Revised: February 5, 2024
Published online:

[1] V. Forti, C. P. Balde, R. Kuehr, G. Bel, The Global E-waste Monitor, UNU/UNITAR SCYCLE, ITU, ISWA, **2020**.
[2] S. Nandy, E. Fortunato, R. Martins, *Prog. Nat. Sci.: Mater. Int.* **2022**, *32*, 1.
[3] A. R. Brown, G. Whale, M. Jackson, S. Marshall, M. Hamer, A. Solga, P. Kabouw, M. Galay-Burgos, R. Woods, S. Nadzialek, L. Maltby, *Integr. Environ. Assess. Manage.* **2017**, *13*, 17.
[4] V. Skákalová, A. B. Kaiser, *Graphene: Properties, Preparation, Characterization and Applications*, Woodhead Publishing, Sawston, Cambridge **2021**.
[5] D. Beloin-Saint-Pierre, R. Hischier, *Int. J. Life Cycle Assess.* **2021**, *26*, 327.
[6] A. Razaq, F. Bibi, X. Zheng, R. Papadakis, S. H. M. Jafri, H. Li, *Materials* **2022**, *15*, 1012.
[7] R. Ye, D. K. James, J. M. Tour, *Adv. Mater.* **2019**, *31*, 1803621.
[8] R. Ye, D. K. James, J. M. Tour, *Acc. Chem. Res.* **2018**, *51*, 1609.
[9] M. Wang, Y. Yang, W. Gao, *Trends Chem.* **2021**, *3*, 969.
[10] F. J. Romero, E. Castillo, A. Rivadeneyra, A. Toral-Lopez, M. Becherer, F. G. Ruiz, N. Rodriguez, D. P. Morales, *npj Flexible Electron.* **2019**, *3*, 12.
[11] J. Lin, Z. Peng, Y. Liu, F. Ruiz-Zepeda, R. Ye, E. L. Samuel, M. J. Yacaman, B. I. Yakobson, J. M. Tour, *Nat. Commun.* **2014**, *5*, 1.
[12] Y. Houeix, F. J. Romero, C. L. Moraila, A. Rivadeneyra, N. Rodriguez, D. P. Morales, A. Salinas-Castillo, *Appl. Surf. Sci.* **2023**, *634*, 157629.
[13] B. Kulyk, B. F. Silva, A. F. Carvalho, S. Silvestre, A. J. Fernandes, R. Martins, E. Fortunato, F. M. Costa, *ACS Appl. Mater. Interfaces* **2021**, *13*, 10210.
[14] Y.-J. Kim, T.-S. D. Le, H. K. Nam, D. Yang, B. Kim, *CIRP Ann.* **2021**, *70*, 443.
[15] A. Imbrogno, J. Islam, C. Santillo, R. Castaldo, L. Sygellou, C. Larrigy, R. Murray, E. Vaughan, M. K. Hoque, A. J. Quinn, D. Iacopino, *ACS Appl. Electron. Mater.* **2022**, *4*, 1541.
[16] P. I. C Claro, T. Pinheiro, S. L. Silvestre, A. C. Marques, J. Coelho, J. M. Marconcini, E. Fortunato, L. H. C Mattoso, R. Martins, *Appl. Phys. Rev.* **2022**, *9*.
[17] A. C. Bressi, A. Dallinger, Y. Steksova, F. Greco, *ACS Appl. Mater. Interfaces* **2023**, *15*, 35788.
[18] Y. Chyan, R. Ye, Y. Li, S. P. Singh, C. J. Arnusch, J. M. Tour, *ACS Nano* **2018**, *12*, 2176.
[19] S. Silva, M. Sabino, E. Fernandes, V. Correlo, L. Boesel, R. L. Reis, *Int. Mater. Rev.* **2005**, *50*, 345.
[20] E. Vaughan, C. Santillo, M. Setti, C. Larrigy, A. J. Quinn, G. Gentile, M. Lavorgna, D. Iacopino, *Adv. Sens, Res.* **2023**, 2300026.
[21] S. L. Silvestre, T. Pinheiro, A. C. Marques, J. Deuermeier, J. Coelho, R. Martins, L. Pereira, E. Fortunato, *Flexible Printed Electron.* **2022**, *7*, 035021.
[22] A. F. Carvalho, A. J. Fernandes, R. Martins, E. Fortunato, F. M. Costa, *Adv. Mater. Technol.* **2020**, *5*, 2000630.
[23] M. A. Najeeb, Z. Ahmad, R. A. Shakoor, *Adv. Mater. Interfaces* **2018**, *5*, 1800969.
[24] C. Sun, Q. Shi, M. S. Yazici, C. Lee, Y. Liu, *Sensors* **2018**, *18*, 4352.
[25] T. Delipinar, A. Shafique, M. S. Gohar, M. K. Yapici, *ACS Omega* **2021**, *6*, 8744.
[26] C. Zhang, J. Ping, Y. Ying, *Sci. Total Environ.* **2020**, *714*, 136687.
[27] L. Lan, X. Le, H. Dong, J. Xie, Y. Ying, J. Ping, *Biosens. Bioelectron.* **2020**, *165*, 112360.
[28] Y. Lu, G. Yang, Y. Shen, H. Yang, K. Xu, *Nano-Micro Lett.* **2022**, *14*, 150.
[29] S. Zou, L.-Q. Tao, G. Wang, C. Zhu, Z. Peng, H. Sun, Y. Li, Y. Wei, T.-L. Ren, *ACS Appl. Mater. Interfaces* **2022**, *14*, 12606.
[30] K. Liu, B. Ouyang, X. Guo, Y. Guo, Y. Liu, *npj Flexible Electron.* **2022**, *6*, 1.
[31] B. Arman Kuzubasoglu, *ACS Appl. Electron. Mater.* **2022**, *4*, 4797.
[32] C. Huang, M. Jiang, F. Liu, *ACS Appl. Electron. Mater.* **2023**, *5*, 4067.
[33] X. Fan, K. Elgammal, A. D. Smith, M. Östling, A. Delin, M. C. Lemme, F. Niklaus, *Carbon* **2018**, *127*, 576.
[34] C. Lv, C. Hu, J. Luo, S. Liu, Y. Qiao, Z. Zhang, J. Song, Y. Shi, J. Cai, A. Watanabe, *Nanomaterials* **2019**, *9*, 422.
[35] P. Songkeaw, K. Onlaor, T. Thiwawong, B. Tunhoo, *J. Mater. Sci.: Mater. Electron.* **2020**, *31*, 12206.
[36] A. N. Ghulam, O. A. Dos Santos, L. Hazeem, B. Pizzorno Backx, M. Bououdina, S. Bellucci, *J. Funct. Biomater.* **2022**, *13*, 77.
[37] V. S. Turkani, D. Maddipatla, B. B. Narakathu, T. S. Saeed, S. O. Obare, B. J. Bazuin, M. Z. Atashbar, *Nanoscale Adv.* **2019**, *1*, 2311.
[38] B. Kulyk, B. F. Silva, A. F. Carvalho, P. Barbosa, A. V. Girão, J. Deuermeier, A. J. Fernandes, F. M. Figueiredo, E. Fortunato, F. M. Costa, *Adv. Mater. Technol.* **2022**, *7*, 2101311.
[39] T.-S. D. Le, S. Park, J. An, P. S. Lee, Y.-J. Kim, *Adv. Funct. Mater.* **2019**, *29*, 1902771.
[40] T.-S. D. Le, Y. A. Lee, H. K. Nam, K. Y. Jang, D. Yang, B. Kim, K. Yim, S.-W. Kim, H. Yoon, Y.-J. Kim, *Adv. Funct. Mater.* **2022**, *32*, 2107768.
[41] R. Ye, Y. Chyan, J. Zhang, Y. Li, X. Han, C. Kittrell, J. M. Tour, *Adv. Mater.* **2017**, *29*, 1702211.
[42] M. G. Stanford, J. T. Li, Y. Chyan, Z. Wang, W. Wang, J. M. Tour, *ACS Nano* **2019**, *13*, 7166.

[43] A. Van Eeckhout, E. Garcia-Caurel, T. Garnatje, J. C. Escalera, M. Durfort, J. Vidal, J. J. Gil, J. Campos, A. Lizana, *Sci. Rep.* **2021**, *11*, 3913.
[44] I. Children, L. A. Jauregui, W. Park, H. Cao, Y. P. Chen, New Developments in Photon and Materials Research, **2013**, *1*, 3.
[45] A. C. Ferrari, D. M. Basko, *Nat. Nanotechnol.* **2013**, *8*, 235.
[46] V. T. Nguyen, H. D. Le, V. C. Nguyen, T. T. T. Ngo, D. Q. Le, X. N. Nguyen, N. M. Phan, *Adv. Nat. Sci. Nanosci. Nanotechnol.* **2013**, *4*, 035012.
[47] X. Dong, P. Wang, W. Fang, C.-Y. Su, Y.-H. Chen, L.-J. Li, W. Huang, P. Chen, *Carbon* **2011**, *49*, 3672.
[48] K. Muzyka, G. Xu, *Electroanalysis* **2022**, *34*, 574.
[49] H. Pereira, *BioResources* **2015**, *10*, 6207.
[50] A. Şen, A. V. Marques, J. Gominho, H. Pereira, *Ind. Crops Prod.* **2012**, *38*, 132.
[51] B. Esteves, Y. Dulyanska, C. Costa, J. V. Ferreira, I. Domingos, H. Pereira, L. T. de Lemos, L. V. Cruz-Lopes, *BioResources* **2017**, *12*, 2339.
[52] C. I. Martins, V. Gil, *Front. Mater.* **2020**, *7*, 297.
[53] W. Shangguan, Z. Chen, J. Zhao, X. Song, *Wood Sci. Technol.* **2018**, *52*, 181.
[54] M. Han, W. Shen, *Carbohydr. Polym.* **2022**, *298*, 120109.
[55] M. Kuş, S. Okur, *Sens. Actuators, B* **2009**, *143*, 177.
[56] Y. Chen, M. Li, W. Yan, X. Zhuang, K. W. Ng, X. Cheng, *ACS Omega* **2021**, *6*, 1216.
[57] M. R. Bobinger, F. J. Romero, A. Salinas-Castillo, M. Becherer, P. Lugli, D. P. Morales, N. Rodríguez, A. Rivadeneyra, *Carbon* **2019**, *144*, 116.
[58] A. P. Poeiras, C. Vogel, B. Günther, C. Camilo-Alves, P. Surovỳ, M. E. Silva, N. de Almeida Ribeiro, *Forests* **2022**, *13*, 623.
[59] A. Lagorce-Tachon, T. Karbowiak, D. Champion, R. D. Gougeon, J.-P. Bellat, *Mater. Des.* **2015**, *82*, 148.
[60] A. Rivadeneyra, J. Fernández-Salmerón, M. Agudo, J. A. López-Villanueva, L. F. Capitan-Vallvey, A. J. Palma, *Sens. Actuators, B* **2014**, *195*, 123.
[61] Y. Chen, P. Pötschke, J. Pionteck, B. Voit, H. Qi, *J. Mater. Chem. A* **2018**, *6*, 7777.
[62] P. Zhu, Y. Liu, Z. Fang, Y. Kuang, Y. Zhang, C. Peng, G. Chen, *Langmuir* **2019**, *35*, 4834.
[63] D. Zaharie-Butucel, L. Digianantonio, C. Leordean, L. Ressier, S. Astilean, C. Farcau, *Carbon* **2017**, *113*, 361.
[64] M. Khalifa, G. Wuzella, H. Lammer, A. R. Mahendran, *Synth. Met.* **2020**, *266*, 116420.
[65] Z.-H. Duan, Q.-N. Zhao, C.-Z. Li, S. Wang, Y.-D. Jiang, Y.-J. Zhang, B.-H. Liu, H.-L. Tai, *Rare Met.* **2021**, *40*, 1762.
[66] S. Tachibana, Y.-F. Wang, T. Sekine, Y. Takeda, J. Hong, A. Yoshida, M. Abe, R. Miura, Y. Watanabe, D. Kumaki, S. Tokito, *ACS Appl. Mater. Interfaces* **2022**, *14*, 5721.
[67] X. Yao, L. Chen, Z. Luo, C. Ye, F. Liang, T. Yang, X. Liu, X. Tian, H. Bi, C. Wang, C. Cai, L. Lyu, X. Wu, *Nano Select* **2022**, *3*, 1168.
[68] J. I. Fernandez-Golfin Seco, M. Conde García, F. Gonzalez Hernandez, M. Conde García, J. J. Fernandez-Golfin Seco, V. Baonza Merino, L. García Esteban, J. R. Gonzalez Adrados, *For. Syst.* **2010**, *19*, 184.
[69] J. B. Engel, C. L. Luchese, I. C. Tessaro, *J. Food Eng.* **2022**, *328*, 111063.
[70] Standard Test Method for Sheet Resistance Uniformity Evaluation by In-Line Four-Point Probe with the Dual-Configuration Procedure, American society for testing and materials **1997**, *10*, 13.